2D Materials

PAPER • OPEN ACCESS

Low-temperature monoclinic layer stacking in atomically thin CrI_3 crystals

To cite this article: Nicolas Ubrig *et al* 2020 *2D Mater.* **7** 015007

IOP Publishing 2D Mater. 7 (2020) 015007 https://doi.org/10.1088/2053-1583/ab4c64

2D Materials

OPEN ACCESS

RECEIVED
23 July 2019

ACCEPTED FOR PUBLICATION
9 October 2019

PUBLISHED
4 November 2019

PAPER

Low-temperature monoclinic layer stacking in atomically thin CrI_3 crystals

Nicolas Ubrig[1,2], Zhe Wang[1,2,3], Jérémie Teyssier[1,2], Takashi Taniguchi[4], Kenji Watanabe[4], Enrico Giannini[1], Alberto F Morpurgo[1,2] and Marco Gibertini[1,5]

[1] Department of Quantum Matter Physics, University of Geneva, 24 Quai Ernest Ansermet, CH-1211 Geneva, Switzerland
[2] Group of Applied Physics, University of Geneva, 24 Quai Ernest Ansermet, CH-1211 Geneva, Switzerland
[3] MOE Key Laboratory for Nonequilibrium Synthesis and Modulation of Condensed Matter, School of Science, Xi'an Jiaotong University, Xi'an 710049, People's Republic of China
[4] National Institute for Materials Science, 1-1 Namiki, Tsukuba, 305-0044, Japan
[5] National Centre for Computational Design and Discovery of Novel Materials (MARVEL), École Polytechnique Fédérale de Lausanne, CH-1015 Lausanne, Switzerland

E-mail: nicolas.ubrig@unige.ch and marco.gibertini@unige.ch

Keywords: Raman spectroscopy, CrI_3, 2D magnetism

Abstract

Chromium triiodide, CrI_3, is emerging as a promising magnetic two-dimensional semiconductor where spins are ferromagnetically aligned within a single layer. Potential applications in spintronics arise from an antiferromagnetic ordering between adjacent layers that gives rise to spin filtering and a large magnetoresistance in tunnelling devices. This key feature appears only in thin multilayers and it is not inherited from bulk crystals, where instead neighbouring layers share the same ferromagnetic spin orientation. This discrepancy between bulk and thin samples is unexpected, as magnetic ordering between layers arises from exchange interactions that are local in nature and should not depend strongly on thickness. Here we solve this controversy and show through polarization resolved Raman spectroscopy that thin multilayers do not undergo a structural phase transition typical of bulk crystals. As a consequence, a different stacking pattern is present in thin and bulk samples at the temperatures at which magnetism sets in and, according to previous first-principles simulations, this results in a different interlayer magnetic ordering. Our experimental findings provide evidence for the strong interplay between stacking order and magnetism in CrI_3, opening interesting perspectives to design the magnetic state of van der Waals multilayers.

The discovery of magnetic order [1, 2] has disclosed novel opportunities in the field of two dimensional (2D) van der Waals crystals and heterostructures [3–5]. In many cases [2, 6, 7], the magnetic configuration of thin layers is the same as in the 3D parent compounds, although possibly with a reduced critical temperature owing to the larger sensitivity of 2D magnets to thermal fluctuations. This is expected as the intra- and inter-layer exchange interactions that determine the ground-state magnetic configuration are typically local and do not change significantly when thinning down the material.

A surprising exception is represented by chromium triiodide, CrI_3, a van der Waals material that in its bulk form shows ferromagnetic (FM) ordering both within and between layers below a critical temperature $T_c \simeq 61$ K [8, 9]. Recently, a multitude of experiments, ranging from magneto-optical Kerr effect measurements [1, 10] to tunnelling magnetotransport [10–13] and scanning magnetometry [14], have shown unarguably that instead thin samples up to at least ~10 layers display an antiferromagnetic (AFM) interlayer exchange coupling between the FM layers. The AFM ordering can be manipulated through external electric fields [15] or doping [16] and it is responsible for a spin-filtering effect on electrons tunnelling through CrI_3 barriers, giving rise to a record-high magnetoresistance [10–13] with potential application in spin transistors [17, 18].

In an attempt to clarify this unexpected change in magnetic ordering from bulk to few layers, most theoretical investigations have focused on the presence of a structural phase transition in bulk CrI_3 at about 200–220 K [8, 19]. Across this transition, the structure evolves from a high-temperature monoclinic phase (figure 1(a), space group $C2/m$) to a rhombohedral

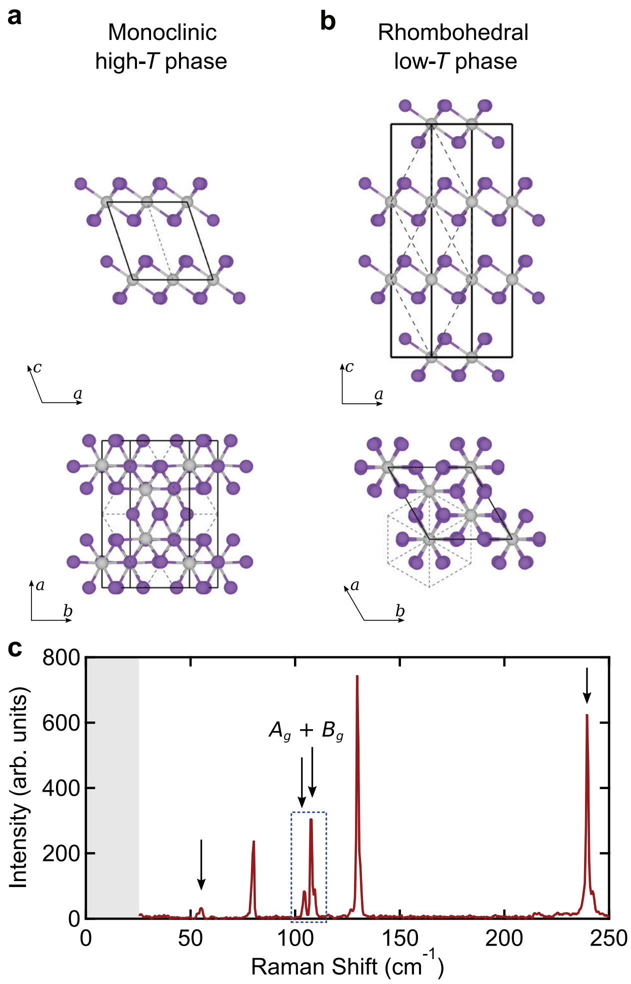

Figure 1. Lateral and top views of the crystal structure of CrI_3 in the monoclinic (high temperature) phase (a) and in the rhombohedral (low temperature) phase (b). Both the primitive (thin dashed line) and the conventional (thick solid line) unit cells are reported. (c) Typical Raman spectrum of bulk CrI_3 at room temperature without resolving the polarization. The black arrows indicate the pairs of A_g and B_g vibrational modes sensitive to the structural phase transition. The blue dashed rectangle highlights the Raman active modes on which we focus our attention in the following.

structure (figure 1(b), space group $R\bar{3}$) at low temperature, with the main distinction between the two phases being a different stacking order of the layers. First-principles simulations in [12], corroborated by additional theoretical investigations [20–24], have shown that the interlayer exchange coupling is FM in the rhombohedral phase (in agreement with experimental observations for bulk CrI_3), while it is AFM in the monoclinic structure. The strong interplay between stacking order and magnetic configuration suggests a possible scenario to solve the conundrum: if thin samples exfoliated at room temperature from bulk monoclinic crystals are not able to undergo a structural phase transition, they remain in the metastable monoclinic phase and are thus expected to display AFM ordering at low temperature.

This picture is in agreement with recent measurements on few-layer CrI_3 where either an accidental puncture [14] or an external pressure [25, 26] provided the energy to undergo a structural transformation with a corresponding transition to FM ordering. Additional validations supporting the connection between crystal structure and magnetism have been achieved in a related material, $CrBr_3$, by observing different magnetic ordering associated with novel stacking patterns (not corresponding to the bulk phases) in bilayers grown by molecular beam epitaxy [27]. The ultimate confirmation of the proposed scenario requires a technique sensitive to the stacking order of few layer structures in order to verify the absence of structural phase transitions in few layers. In this regard, second-harmonic generation is an effect which is sensitive to the different crystal symmetry in the two phases and that has been recently adopted [28] to show that bilayer CrI_3 remains monoclinic down to very low temperature. Alternatively, another practical approach that has been successfully employed [29] in a similar material, $CrCl_3$, relies on polarization resolved Raman spectroscopy.

In this work, we show the absence of structural phase transitions in thin CrI_3 through polarization resolved Raman spectroscopy. Based on general symmetry arguments, we develop a strategy to distinguish the monoclinic and rhombohedral phases by looking at the angular dependence of the Raman response to linearly polarized light. We validate this approach for

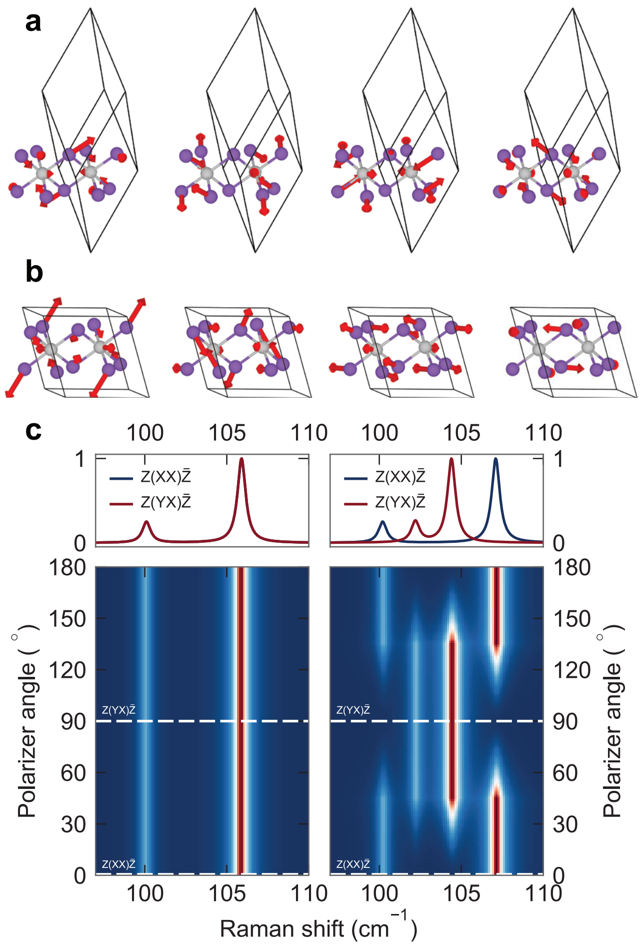

Figure 2. Phonon displacement pattern according to first-principles simulations of the modes visible in the Raman spectrum close to 100 cm^{-1} either in the rhombohedral (a) or monoclinic (b) phase. The modes appear in order of increasing frequency. (c) Colour plot of the normalized Raman spectrum as a function of the polarization angle and Raman shift. Results for both the rhombohedral (left) and monoclinic (right) phase of bulk CrI_3 are reported. Here we assume that the polarization angle of the incident light θ_I is varied, while keeping the detector for the scattered light fixed at $\theta_S = 0$. Intensities and vibrational frequencies are computed from first principles as detailed in the Methods, although the position of the brightest A_g and B_g modes of the monoclinic structure (as well as the corresponding E_g mode in the rhombohedral phase) have been displaced by 4 cm^{-1} to obtain a better qualitative agreement with experiments (see below). The upper insets show the Raman spectra in parallel (blue) or cross (red) polarization, corresponding to the horizontal dashed lines in the colour plots.

bulk crystals by evidencing the existence of a monoclinic phase at high temperature and a rhombohedral one at low temperature, in agreement with the general understanding. Raman measurements on encapsulated CrI_3 multilayers on the contrary show that thin crystals remain in the monoclinic phase even when the sample is cooled down to base temperature. This has crucial implications on the magnetic ground state of atomically thin samples, which is very sensitive to the stacking order of the layers, and finally explains the controversial AFM ordering observed in experiments.

Methods

CrI_3 crystals are grown by the chemical vapor transport method and, owing to the enormous sensitivity of this material to atmosphere, stored in a nitrogen-gas-filled glove box with sub-ppm concentration of O_2 and H_2O. The investigated bulk crystals are freshly cleaved, mounted on a He-flow cryostat (cryovac KONTI cryostat) in the glove box, and sealed in the vacuum chamber with optical access before being transferred to the optical setup. The nm-thick multilayers of CrI_3 are obtained by mechanical exfoliation with scotch tape. The flakes are then picked up with standard dry transfer techniques and fully encapsulated in 10–30 nm thick exfoliated hBN. The samples are removed from the glovebox and placed into the cryostat for optical investigations.

All Raman spectroscopy measurements in this work are performed using a Horiba scientific (LabRAM HR Evolution) confocal microscope in backscattering geometry. The nominal laser power before the microscope objective and the window of the cryostat is 60 μW and the excitation wavelength 532 nm. After laser excitation the dispersed light is sent to a Czerni–Turner spectrometer equipped with a 1800 groves mm^{-1} grating, which resolves the optical spectra with a precision of 0.3 cm^{-1}. The light is detected with the help of a N_2-cooled CCD-array. The incident linear polarization of the laser is varied using a $\lambda/2$-plate while the analyzer, placed on the detecting light path, is kept fix.

First-principles simulations have been performed within density functional theory using the Quantum ESPRESSO suite of codes [30, 31]. In order to treat magnetism and van der Waals interactions on an equal footing we have adopted the spin-polarized extension [32] of the van der Waals density functional (vdw-DF) method [33, 34]. The unit cell is kept fixed to the experimentally reported structure [8] for both the rhombohedral and monoclinic phase, while atomic positions have been relaxed so that any component of the force on any atom does not exceed 2.5×10^{-3} eV $\mathring{\mathrm{A}}^{-1}$. Phonon frequencies at vanishing wave vector have been then computed by finite differences using the phonopy software [35]. From the computed phonon displacement patterns, the Raman tensors have been calculated within the Placzec approximation as derivatives of the electronic contribution to the dielectric tensor with respect to the phonon amplitude, again using finite differences. In all calculations, we adopt pseudopotentials from the Standard Solid State Pseudopotential Library (SSSP) [36], with a cutoff of 60 Ry for wavefunctions and 480 Ry for the charge density. The Brillouin zone corresponding to the primitive unit cell is sampled using a regular Monkhorst–Pack grid centered at Γ with $8 \times 8 \times 8$ or $6 \times 6 \times 6$ k-points in either the monoclinic or rhombohedral phase.

Results and discussion

Figure 1(c) shows a typical Raman spectrum of bulk $\mathrm{CrI_3}$ at room temperature, in agreement with previous literature [19]. The visible modes belong to either one of two possible irreducible representations, A_g or B_g, of the $2/m$ (or C_{2h}) point group corresponding to the high-temperature phase. When the structure undergoes a transition to the rhombohedral phase, some pairs of A_g and B_g modes (highlighted in figure 1) become degenerate and transform according to the two-dimensional E_g irreducible representation of the low-temperature $\bar{3}$ (or C_{3i}) point group. The presence of degenerate or split modes thus represents a potential signature to distinguish between the two structural phases and to track the phase transition. Still, the frequency separation between the split modes is typically very small [19] (few cm^{-1}) and thus expected to get harder to be visible in unpolarized Raman spectra when the thickness of the sample is narrowed down and the signal gets weaker.

Such difficulty can be overcome in polarization resolved Raman spectroscopy by exploiting the different Raman response of A_g, B_g, and E_g modes to polarized light. Indeed, as we shall see, the dependence on the polarization angle cancels out when the contribution from the two degenerate modes forming a E_g peak is summed over in the rhombohedral phase, resulting in a constant spectrum insensitive to the polarization configuration. On the contrary, in the monoclinic structure the A_g and B_g modes that result from the splitting of the degenerate E_g peak have opposite response, giving rise to two peaks with an intensity that oscillates out of phase with the polarization angle, so that the close A_g and B_g peaks are much easier to resolve [19, 29].

To provide a rigorous foundation of this procedure, we first recall that in non-resonant Stokes conditions, the Raman spectrum can be expressed as

$$I(\omega) = I_0 \sum_{\nu} \frac{\omega_I \omega_S^3}{\omega_\nu} \mid \boldsymbol{\epsilon}_S \cdot \overleftrightarrow{\boldsymbol{R}}^{\nu} \cdot \boldsymbol{\epsilon}_I \mid^2 [n_\nu + 1] \delta(\omega - \omega_\nu), \tag{1}$$

where the line-shape has been simplified to a δ-function, ω is the Raman shift, ω_ν is the frequency of the νth long-wavelength phonon mode, $\boldsymbol{\epsilon}_I$ and $\boldsymbol{\epsilon}_S$ the polarization vectors of the incident and scattered light with frequency ω_I and $\omega_S = \omega_I - \omega$, and $n_\nu = [\exp(\hbar\omega_\nu/(k_\mathrm{B}T)) - 1]^{-1}$ is the Bose–Einstein occupation of the νth mode. Based on symmetry arguments, the Raman tensors $\overleftrightarrow{\boldsymbol{R}}^{\nu}$ entering equation (1) have the following general expressions for modes belonging to the A_g or B_g representations of the high-temperature point group

$$\overleftrightarrow{\boldsymbol{R}}^{A_g} = \begin{pmatrix} a & 0 & d \\ 0 & c & 0 \\ d & 0 & b \end{pmatrix} \qquad \overleftrightarrow{\boldsymbol{R}}^{B_g} = \begin{pmatrix} 0 & e & f \\ e & 0 & 0 \\ f & 0 & 0 \end{pmatrix} \tag{2}$$

and

$$\overleftrightarrow{\boldsymbol{R}}^{\,^1E_g} = \begin{pmatrix} m & n & p \\ n & -m & q \\ p & q & 0 \end{pmatrix} \qquad \overleftrightarrow{\boldsymbol{R}}^{\,^2E_g} = \begin{pmatrix} n & -m & -q \\ -m & -n & p \\ -q & p & 0 \end{pmatrix} \tag{3}$$

for pairs of degenerate modes belonging to the E_g representation of the low-temperature point group.

To identify a strategy to distinguish the two phases, we focus on the most common back-scattering geometry with linearly polarized light, whose polarization vectors can thus be written as $\boldsymbol{\epsilon}_{I/S} = (\cos\theta_{I/S}, \sin\theta_{I/S}, 0)$. To simplify the derivation we observe that, as the degenerate E_g modes split into a A_g and a B_g mode, we expect $a \approx -c$ (and $|a| \approx |e|$), so that $R^{\nu}_{yy} \approx -R^{\nu}_{xx}$ for all the modes considered here. As a consequence, we find

$$\begin{aligned} \boldsymbol{\epsilon}_S \cdot \overleftrightarrow{\boldsymbol{R}}^{\nu} \cdot \boldsymbol{\epsilon}_I &= \cos\theta_S \cos\theta_I R^{\nu}_{xx} + \sin\theta_S \sin\theta_I R^{\nu}_{yy} \\ &\quad + \sin(\theta_S + \theta_I) R^{\nu}_{xy} \\ &= \cos\theta R^{\nu}_{xx} + \sin\theta R^{\nu}_{xy}, \end{aligned} \tag{4}$$

yielding an intensity in equation (1) that can be written in terms of the cumulative angle $\theta = \theta_S + \theta_I$. From the general expressions for the Raman tensors, we find that the Raman spectrum is completely independent of the polarization angles close to a degenerate E_g peak in the low-temperature phase,

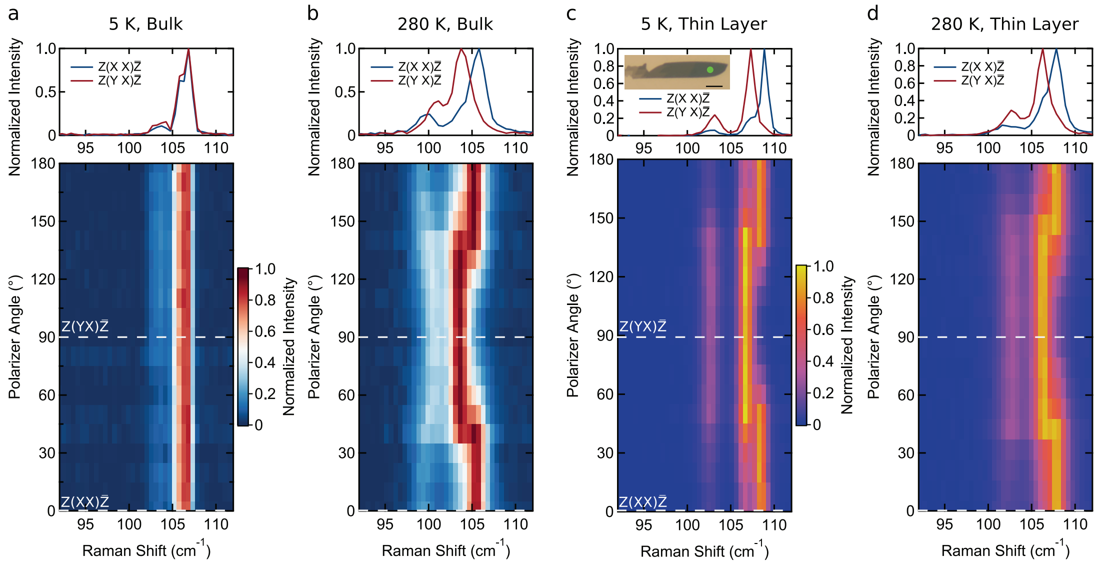

Figure 3. Colour plots of the normalized intensity as a function of the Raman shift (in cm^{-1}) in the investigated frequency region and of the angle of the incoming linearly polarized light. The white dashed lines indicate co- and cross-polarized configurations ($Z(XX)\bar{Z}$ and $Z(YX)\bar{Z}$, respectively). The top panels show individual line cuts for $Z(XX)\bar{Z}$ and $Z(YX)\bar{Z}$. Bulk $\mathrm{CrI_3}$ at $T=5$ K (a) and $T=280$ K (b) show excellent agreement with the theoretical predictions showing that the structural phase transition from monoclinic, at high temperatures, to rhombohedral, at low temperatures, takes place. The experimental data for a 4 nm thick crystal of $\mathrm{CrI_3}$ is shown in (c) and (d) for $T=5$ K and $T=280$ K, respectively. The area probed here and an optical micrograph of the flake is depicted in the inset of panel (c). The scale bar corresponds to 10 μm. Except for a slight stiffening of the modes due to the decreased temperature we do not observe significant differences between the experimental data at low and high temperatures. In particular, the polarization pattern is virtually identical, indicating that no structural transition occurs so that the system remains in the monoclinic phase down to low temperature.

$$I_{E_g}(\omega)=I_0\frac{\omega_I(\omega_I-\omega)^3}{\omega_{E_g}}[n_{E_g}+1](m^2+n^2)\delta(\omega-\omega_{E_g}) \tag{5}$$

while the intensity of the split A_g and B_g modes of the monoclinic structure oscillates out of phase as a function of the angle θ:

$$I_{A_g+B_g}(\omega)=I_0\omega_I(\omega_I-\omega)^3a^2 \times\left[\frac{n_{A_g}+1}{\omega_{A_g}}\cos^2\theta\delta(\omega-\omega_{A_g})+\frac{n_{B_g}+1}{\omega_{B_g}}\sin^2\theta\delta(\omega-\omega_{B_g})\right]. \tag{6}$$

This provides us with a strategy to distinguish the two structural phases by looking at the evolution of the Raman spectrum as the cumulative polarization angle θ is varied, e.g. by keeping fixed θ_S while sweeping θ_I. In the rhombohedral phase we expect degenerate E_g peaks whose intensity and frequency position do not change with the polarization angle, while the monoclinic structure is characterized by pairs of close peaks associated with A_g and B_g modes whose intensity alternates out of phase as a function of θ, enhancing the visibility of the split modes even when the frequency separation is very small. In the following we focus on the spectral range around 100 cm^{-1}, where this strategy is particularly suitable owing to the presence [19] of two nearby E_g modes in the rhombohedral phase split into two pairs of A_g+B_g modes in the monoclinic phase.

The procedure is exemplified in figure 2 in a model calculation, where the Raman intensities and vibrational frequencies have been computed for the rhombohedral and monoclinic structures from first principles (see Methods), although the position of the strongest A_g+B_g peaks of the monoclinic crystal (and for consistency also the corresponding E_g peak in the rhombohedral phase) have been shifted by 4 cm^{-1} to result in a better qualitative agreement with experiments. The angular dependence of the two spectra are clearly different, supporting the effectiveness of our strategy to distinguish the two structural phases. Indeed, as expected from the above discussion, for the rhombohedral structure, the Raman spectrum is insensitive to the polarization angle θ_I (here we assume $\theta_S=0$), while in the monoclinic phase we have a transfer of spectral intensity as a function of θ_I between two peaks of a split A_g+B_g pair. In particular, this results into very different spectra in parallel configuration ($\theta_I=\theta_S=0$, or $Z(XX)\bar{Z}$ in Porto notation), where only A_g modes are visible, or cross configuration ($\theta_I=\pi/2$, or $Z(YX)\bar{Z}$), where only B_g modes are present, allowing to clearly resolve their frequency separation.

We first validate our approach by considering bulk samples, for which a structural phase transition is expected to occur at 200–220 K and should manifest itself in a change of the angular dependence of the Raman spectrum. Figure 3(a, b) shows the Raman response measured at two different temperatures, above and below the structural phase transition, as a function of the polarization angle θ_I of the incident light, while the detecting polarizer is kept fixed (see Methods). At 5 K a weak and a strong peak are present at 103 and 107 cm^{-1} respectively, and their intensity does not evolve with θ_I, clearly showing that these are E_g modes of the rhombohedral structure.

In particular, the relative intensity of the two modes is in very good agreement with the first-principles results in figure 2 and allows us to make a more definite assignment of the corresponding phonon patterns. At high temperature (280 K), each peak splits into two with intensities that oscillate out of phase as a function of θ_I, so that for parallel and cross polarization (upper panel) only one of the two split modes is visible. This is exactly what is predicted for a monoclinic structure in figure 2 and we can thus unambiguously identify the peaks as pairs of $A_g + B_g$ modes, indicating that the structure is monoclinic at high temperature. Our approach thus confirms that bulk crystals undergo a structural transition from a monoclinic phase at high temperature to a rhombohedral phase at low temperature.

We are now in a position to consider thin samples obtained by mechanical exfoliation (see Methods). Figure 3(c, d) shows the Raman spectra obtained at 5 and 280 K for a 4 nm thick CrI_3 crystal (see inset, approximately six layers) as a function of the polarization angle. For definiteness, we focus on the same spectral range considered for bulk samples. In this case, apart from a clear reduction of the peak width upon decreasing temperature, the two spectra are virtually identical. In particular, both at high and low temperature we find two pairs of close by peaks whose intensity varies with the polarization angle in phase opposition. Such transfer of spectral intensity as a function of θ_I between nearby peaks is the clear signature of the monoclinic phase introduced before, ruling out the emergence of the rhombohedral phase.

As temperature plays a crucial role in the rhombohedral-monoclinic transition, sound conclusions on the presence or absence of structural changes require an independent cross check of the effective temperature of the sample for every experiment. Indeed, in a measurement of the Raman spectrum of insulators—which usually have low thermal conductivity—the laser can heat up the illuminated sample area. For instance the temperature can be lifted locally above a phase transition temperature, potentially leading to spectra that artificially look similar even at very different nominal temperatures [29]. Through the analysis of the intensity ratio between the Stokes and the anti-Stokes peaks in the entire spectral range [37] we ensure that the sample area which is probed remains below the temperatures of the phase transitions.

We can thus safely state that thin samples remain in the monoclinic structure down to very low temperature, even below the critical temperature T_c at which magnetism sets in. In this respect, the persistence of the monoclinic phase explains the observation [10–13] of layer antiferromagnetism in thin crystals, as opposed to the bulk FM order. Indeed, the monoclinic stacking order has been predicted to favour an AFM interlayer exchange coupling according to density-functional-theory simulations [12, 20–24]. The different magnetic state also results in a change in critical temperature, from 61 K in the bulk to 51 K [12] in thin crystals.

Remarkably, this reduced T_c matches exactly the temperature at which an anomaly is observed [8, 12] in the magnetization curves of bulk CrI_3. This could indicate that also the outermost layers of bulk samples do not undergo a structural transition, in the same way as thin crystals. Indeed, by remaining in the monoclinic phase, such layers would display AFM order, giving rise to an anomaly at the onset of antiferromagnetism in monoclinic CrI_3 (51 K instead of 61 K), which corresponds to the temperature of the anomaly observed in experiments.

The common behaviour of thin crystals and the outermost layers of bulk CrI_3 would then suggest the importance of free surfaces in the suppression of the structural transition. Indeed, the absence of neighbouring layers at the surface could affect both the thermodynamics and the kinetics of the phase transition, e.g. by changing the vibrational free energy or the barrier height. Such effects could extend quite deeply inside the material or for relatively large thicknesses. Although this seems promising, further studies will be needed to clarify the precise nature and the spatial extension of the surface effects on the structural transition.

Conclusion

In conclusion, we have identified a strategy to distinguish between the two structural phases of CrI_3 through polarization resolved Raman spectroscopy. We have validated our approach in the case of bulk crystals, confirming the existence of a structural transition from a monoclinic phase at high temperature to a rhombohedral phase at low temperature. When considering thin samples, our Raman spectroscopy analysis shows that the monoclinic structure persists down to very low temperature, clearly indicating the absence of any structural change when the thickness of the material is narrowed to few atomic layers. These results provide fundamental insight to confirm a plausible scenario that explains the full set of experimental data on CrI_3, possibly including the presence of anomalies in the magnetization curves of bulk crystals.

Note. During the preparation of this manuscript we became aware that Raman results similar to the ones reported here have very recently appeared in [26].

Acknowledgments

We sincerely acknowledge Alexandre Ferreira for technical support. AFM gratefully acknowledges financial support from the Swiss National Science Foundation (Division II) and from the EU Graphene Flagship project. MG acknowledges support from the Swiss National Science Foundation through the

Ambizione program. Simulation time was provided by CSCS on Piz Daint (project IDs s825 and s917). KW and TT acknowledge support from the Elemental Strategy Initiative conducted by the MEXT, Japan, A3 Foresight by JSPS and the CREST (JPMJCR15F3), JST. ZW acknowledges support from the National Natural Science Foundation of China (Grants No. 11904276).

ORCID iDs

Nicolas Ubrig https://orcid.org/0000-0002-1966-4435
Zhe Wang https://orcid.org/0000-0001-5664-2932
Jérémie Teyssier https://orcid.org/0000-0002-7590-2987
Takashi Taniguchi https://orcid.org/0000-0002-1467-3105
Kenji Watanabe https://orcid.org/0000-0003-3701-8119
Enrico Giannini https://orcid.org/0000-0003-3536-4771
Alberto F Morpurgo https://orcid.org/0000-0003-0974-3620
Marco Gibertini https://orcid.org/0000-0003-3980-5319

References

[1] Huang B *et al* 2017 Layer-dependent ferromagnetism in a van der Waals crystal down to the monolayer limit *Nature* **546** 270
[2] Gong C *et al* 2017 Discovery of intrinsic ferromagnetism in two-dimensional van der Waals crystals *Nature* **546** 265
[3] Burch K S, Mandrus D and Park J-G 2018 Magnetism in two-dimensional van der Waals materials *Nature* **563** 47
[4] Gong C and Zhang X 2019 Two-dimensional magnetic crystals and emergent heterostructure devices *Science* **363** eaav4450
[5] Gibertini M, Koperski M, Morpurgo A F and Novoselov K S 2019 Magnetic 2D materials and heterostructures *Nat. Nanotechnol.* **14** 408
[6] Deng Y *et al* 2018 Gate-tunable room-temperature ferromagnetism in two-dimensional Fe_3GeTe_2 *Nature* **563** 94
[7] Fei Z *et al* 2018 Two-dimensional itinerant ferromagnetism in atomically thin Fe_3GeTe_2 *Nat. Mater.* **17** 778
[8] McGuire M A, Dixit H, Cooper V R and Sales B C 2015 Coupling of crystal structure and magnetism in the layered, ferromagnetic insulator CrI_3 *Chem. Mater.* **27** 612
[9] Dillon J F and Olson C E 1965 Magnetization, resonance, and optical properties of the ferromagnet CrI_3 *J. Appl. Phys.* **36** 1259
[10] Song T *et al* 2018 Giant tunneling magnetoresistance in spin-filter van der Waals heterostructures *Science* **360** 1214
[11] Klein D R *et al* 2018 Probing magnetism in 2D van der Waals crystalline insulators via electron tunneling *Science* **360** 1218
[12] Wang Z, Gutiérrez-Lezama I, Ubrig N, Kroner M, Gibertini M, Taniguchi T, Watanabe K, Imamoğlu A, Giannini E and Morpurgo A F 2018 Very large tunneling magnetoresistance in layered magnetic semiconductor CrI_3 *Nat. Commun.* **9** 2516
[13] Kim H H, Yang B, Patel T, Sfigakis F, Li C, Tian S, Lei H and Tsen A W 2018 One million percent tunnel magnetoresistance in a magnetic van der Waals heterostructure *Nano Lett.* **18** 4885
[14] Thiel L, Wang Z, Tschudin M A, Rohner D, Gutiérrez-Lezama I, Ubrig N, Gibertini M, Giannini E, Morpurgo A F and Maletinsky P 2019 Probing magnetism in 2D materials at the nanoscale with single-spin microscopy *Science* **364** 973
[15] Jiang S, Shan J and Mak K F 2018 Electric-field switching of two-dimensional van der Waals magnets *Nat. Mater.* **17** 406
[16] Jiang S, Li L, Wang Z, Mak K F and Shan J 2018 Controlling magnetism in 2D CrI_3 by electrostatic doping *Nat. Nanotechnol.* **13** 549
[17] Jiang S, Li L, Wang Z, Shan J and Mak K F 2019 Spin tunnel field-effect transistors based on two-dimensional van der Waals heterostructures *Nat. Electron.* **2** 159
[18] Song T *et al* 2019 Voltage control of a van der Waals spin-filter magnetic tunnel junction *Nano Lett.* **19** 915
[19] Djurdjić-Mijin S, Šolajić A, Pešić J, Šćć M, Liu Y, Baum A, Petrovic C, Lazarević N and Popović Z V 2018 Lattice dynamics and phase transition in CrI_3 single crystals *Phys. Rev.* B **98** 104307
[20] Sivadas N, Okamoto S, Xu X, Fennie C J and Xiao D 2018 Stacking-dependent magnetism in bilayer CrI_3 *Nano Lett.* **18** 7658
[21] Soriano D, Cardoso C and Fernández-Rossier J 2019 Interplay between interlayer exchange and stacking in CrI_3 bilayers *Solid State Commun.* **299** 113662
[22] Jang S W, Jeong M Y, Yoon H, Ryee S and Han M J 2019 Microscopic understanding of magnetic interactions in bilayer CrI_3 *Phys. Rev. Mater.* **3** 031001
[23] Jiang P, Wang C, Chen D, Zhong Z, Yuan Z, Lu Z-Y and Ji W 2019 Stacking tunable interlayer magnetism in bilayer CrI_3 *Phys. Rev.* B **99** 144401
[24] Lei C, Chittari B L, Nomura K, Banerjee N, Jung J and MacDonald A H 2019 Magnetoelectric response of antiferromagnetic van der Waals bilayers (arXiv:1902.06418)
[25] Song T *et al* 2019 Switching 2D magnetic states via pressure tuning of layer stacking (arXiv:1905.10860)
[26] Li T *et al* 2019 Pressure-controlled interlayer magnetism in atomically thin CrI_3 (arXiv:1905.10905)
[27] Chen W, Sun Z, Gu L, Xu X, Wu S and Gao C 2019 Direct observation of van der Waals stacking dependent interlayer magnetism (arXiv:1906.03383)
[28] Sun Z *et al* 2019 Giant nonreciprocal second-harmonic generation from antiferromagnetic bilayer CrI_3 *Nature* **572** 497
[29] Klein D R *et al* 2019 Enhancement of interlayer exchange in an ultrathin two-dimensional magnet *Nat. Phys.* (https://doi.org/10.1038/s41567-019-0651-0)
[30] Giannozzi P *et al* 2009 Quantum ESPRESSO: a modular and open-source software project for quantum simulations of materials *J. Phys.: Condens. Matter* **21** 395502
[31] Giannozzi P *et al* 2017 Advanced capabilities for materials modelling with Quantum ESPRESSO *J. Phys.: Condens. Matter* **29** 465901
[32] Thonhauser T, Zuluaga S, Arter C A, Berland K, Schröder E and Hyldgaard P 2015 Spin signature of nonlocal correlation binding in metal–organic frameworks *Phys. Rev. Lett.* **115** 136402
[33] Dion M, Rydberg H, Schröder E, Langreth D C and Lundqvist B I 2004 Van der Waals density functional for general geometries *Phys. Rev. Lett.* **92** 246401
[34] Lee K, Murray E D, Kong L, Lundqvist B I and Langreth D C 2010 Higher-accuracy van der Waals density functional *Phys. Rev.* B **82** 081101
[35] Togo A and Tanaka I 2015 First principles phonon calculations in materials science *Scr. Mater.* **108** 1
[36] Prandini G, Marrazzo A, Castelli I E, Mounet N and Marzari N 2018 Precision and efficiency in solid-state pseudopotential calculations *NPJ Comput. Mater.* **4** 72
[37] McGrane S D, Moore D S, Goodwin P M and Dattelbaum D M 2014 Quantitative tradeoffs between spatial, temporal, and thermometric resolution of nonresonant Raman thermometry for dynamic experiments *Appl. Spectrosc.* **68** 1279